High Spectral Resolution Observations toward Orion BN at 6 μm: No Evidence for Hot Water

The Astrophysical Journal Letters, 865:L18 (6pp), 2018 October 1 https://doi.org/10.3847/2041-8213/aae1ff

High Spectral Resolution Observations toward Orion BN at 6 μm: No Evidence for Hot Water

Nick Indriolo[1], Jonathan C. Tan[2,3], A. C. A. Boogert[4], C. N. DeWitt[5], E. J. Montiel[6], D. A. Neufeld[7], and M. J. Richter[6]
[1] Space Telescope Science Institute, Baltimore, MD 21218, USA
[2] Department of Space, Earth & Environment, Chalmers University of Technology, SE-412 93 Gothenburg, Sweden
[3] Department of Astronomy, University of Virginia, Charlottesville, VA 22904, USA
[4] Institute for Astronomy, University of Hawaii at Manoa, Honolulu, HI 96822, USA
[5] USRA, SOFIA, NASA Ames Research Center MS 232-11, Moffett Field, CA 94035, USA
[6] Department of Physics, University of California Davis, Davis, CA 95616, USA
[7] Department of Physics & Astronomy, Johns Hopkins University, Baltimore, MD 21218, USA
Received 2018 September 6; accepted 2018 September 14; published 2018 September 27

Abstract

The Becklin–Neugebauer (BN) object in Orion has a large proper motion and radial velocity with respect to the gas and other stars in the region where it is presumed to have formed. Multiple dynamical interaction scenarios have been proposed to explain this motion. In one case BN is thought to have interacted with stars in the Trapezium cluster, while in another it is thought to have interacted with source I while deeply embedded in molecular gas. If there is dense gas that has been retained in close proximity to BN, it may be evidence that the latter scenario is favored. We observed BN at high spectral resolution in three windows near 6 μm using the Echelon-Cross-Echelle Spectrograph on board the Stratospheric Observatory for Infrared Astronomy targeting the ν_2 vibrational band of H_2O. Absorption from only three transitions of H_2O is detected, and through kinematic analysis is associated with cool, dense foreground gas, not BN itself. We find no evidence for H_2O absorption or emission at the systemic velocity of BN.

Key words: ISM: molecules

1. Introduction

The Becklin–Neugebauer (BN) object (Becklin & Neugebauer 1967) is a young, massive (8.0–12.6 $M_\odot$; Scoville et al. 1983; Rodríguez et al. 2005) star, with fast motion through the Orion Nebular Cluster (ONC). It has a radial velocity ($v_{\rm LSR} = 23.5 \pm 0.5\,{\rm km\,s^{-1}}$; Plambeck et al. 2013) that differs from that of the Orion molecular cloud ($v_{\rm LSR} \sim 9\,{\rm km\,s^{-1}}$; Melnick et al. 2010), and a high proper motion ($12.6 \pm 0.6\,{\rm mas\,yr^{-1}}$; Rodríguez et al. 2005). This amounts to BN having a 3D velocity of about $30\,{\rm km\,s^{-1}}$ relative to its surroundings (assuming a distance of ~400 pc; Menten et al. 2007, Kounkel et al. 2017), the origin of which is a matter of debate. Two scenarios have been proposed to explain the motion of BN. The first is dynamical ejection from the θ^1Ori C system (now a binary) in the Trapezium region near the center of the ONC about 4000 years ago (Tan 2004). Current properties of the θ^1Ori C system such as orbital binding energy and recoil proper motion can be explained if BN was ejected from the system (see *N*-body simulations of Chatterjee & Tan 2012). Alternatively, Bally & Zinnecker (2005) and Rodríguez et al. (2005) proposed that dynamical interaction of BN, radio source I, and a potential third body (originally proposed to be radio source n) could have produced the high proper motions of BN and source I in roughly opposite directions. Luhman et al. (2017) have found that the third star in this scenario is very likely to be source x, based on a *Hubble Space Telescope* (*HST*)-detected proper motion of this source. Farias & Tan (2018) carried out *N*-body modeling of an ejection of BN and source x from source I, which would then be a hardened or merged binary, concluding that source I would need to be ~20 $M_\odot$, consistent with recent Atacama Large Millimeter/submillimeter Array (ALMA) observations (Bally et al. 2017; Ginsburg et al. 2018).

The ejection or runaway nature of BN is likely connected to the apparently "explosive" outflow from the KL nebula (Allen & Burton 1993). However, there are a number of uncertainties still associated with the above scenarios. In particular, how exactly the "explosive" outflow is launched during the interaction and whether all of the stars—source I, BN, and source x—were originally forming from the KL nebula (i.e., the Orion Hot Core). The presence of dense gas around BN can help constrain these scenarios. For example, if BN was in the process of forming from the KL nebula, then dense gas of its inner accretion disk should have been retained by BN even after ejection. Here we present high spectral resolution observations of BN made at 6 μm covering the ν_2 ro-vibrational band of H_2O, which has previously been used to identify hot, dense gas in close proximity to massive protostars (e.g., Boonman & van Dishoeck 2003; Indriolo et al. 2015).

2. Observations and Data Reduction

BN was observed using the Echelon-Cross-Echelle Spectrograph (EXES; Richter et al. 2010) on board the Stratospheric Observatory for Infrared Astronomy (SOFIA; Young et al. 2012) on 2017 January 26. Spectra were acquired in cross-dispersed high-resolution mode targeting central wavenumbers of 1485.24 $\rm cm^{-1}$, 1639.29 $\rm cm^{-1}$, and 1747.25 $\rm cm^{-1}$ (hereafter referred to as the 6.7 μm, 6.1 μm, and 5.7 μm spectra, respectively). The 6.7 μm spectrum was obtained at an altitude of 37,930 ft (11,561 m), while the 6.1 μm and 5.7 μm spectra were both obtained at an altitude of 40,000 ft (13,106 m). The entrance slit had a width of 1.″24, providing a resolving power (resolution) of ~85,000 ($3.5\,{\rm km\,s^{-1}}$), and a length of about 10″ (varies slightly between settings). To facilitate the removal of telluric emission lines, exposures alternated between on-target and a blank sky position 43″ away. Total, on-target exposure times for

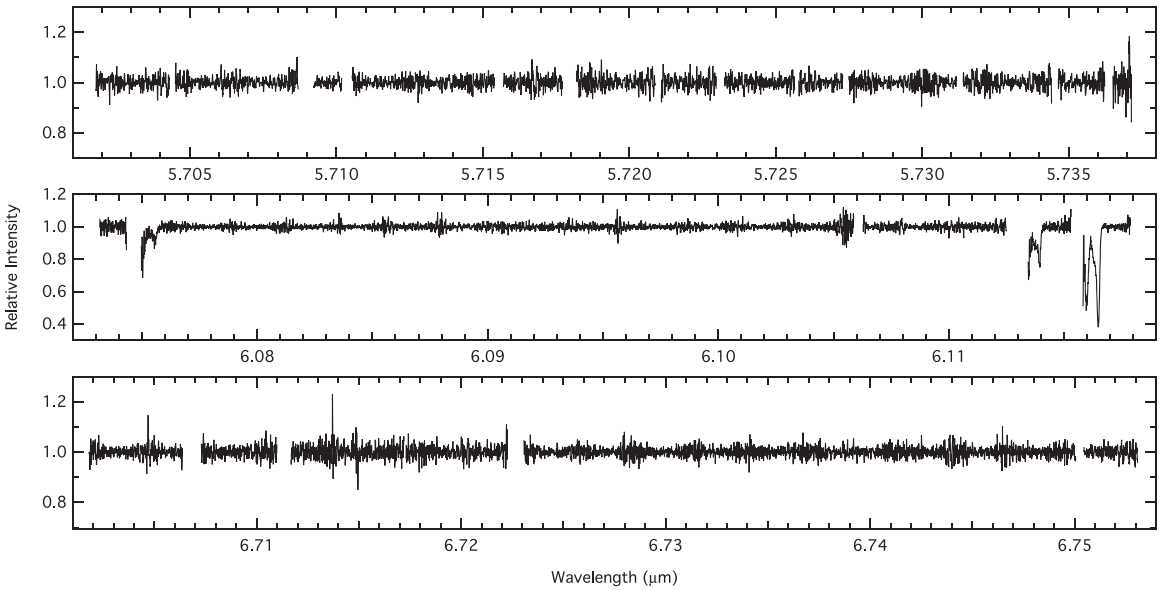

Figure 1. Spectra of BN over the full wavelength range covered by our SOFIA/EXES observations. Each spectrum corresponds to a separate observation at a different grating setting. Oscillations in the noise level result from the cross-dispersed nature of the instrument, with higher noise regions coming from the edges of the individual echelle orders. Gaps in the spectra correspond to regions where telluric water vapor lines reduce transmission levels to near zero. The water absorption lines discussed herein are all from the spectrum in the middle panel.

the 6.7 μm, 6.1 μm, and 5.7 μm spectra were 660 s, 798 s, and 300 s, respectively. Sirius was observed at the same three spectral settings and using the same strategy for use as a telluric standard star.

Data were processed using the `Redux` pipeline (Clarke et al. 2015) with the `fspextool` software package—a modification of the Spextool package (Cushing et al. 2004)—which performs source profile construction, definition of extraction and background apertures, optimal extraction, and wavelength calibration for EXES data. We used this software to produce wavelength calibrated spectra for each individual order of the echellogram. These individual spectra were then stitched together using an average of both orders in the overlap regions to produce a continuous spectrum for each of the three separate observations. To remove baseline fluctuations and atmospheric features the spectra of BN were divided by the corresponding spectra of Sirius using custom macros developed in IGOR Pro[8] that allow for interactive scaling of the atmospheric features in the standard star spectrum to best match those in the science target (McCall 2001). The resulting ratioed spectra were then divided by a 30 pixel boxcar average of the continuum level (extrapolated across absorption lines) to produce the normalized spectra shown in Figure 1.

3. Analysis

Only the 6.1 μm spectrum (middle panel of Figure 1) shows absorption features toward BN; the other two spectra are featureless. Signal-to-noise ratio (S/N) levels on the continuum vary from about 100 to 40 depending on whether the spectrum was observed near the center or edge of an echelle order, respectively. The three detected absorption features are presented in Figure 2, shown in the local standard of rest (LSR) velocity frame for their respective transition wavelengths, and all show multiple absorption components. Absorption from the ν_2 $1_{1,1}$–$0_{0,0}$ water transition out of the ground rotational state is the strongest, with components at 8, 0.5, and -17 km s^{-1}. The other two transitions also show absorption components at 8 and 0.5 km s^{-1}, but the -17 km s^{-1} component in those transitions fell in regions of low atmospheric transmission or poor atmospheric removal. The transmission spectra in Figure 2 were fit using a sum of Gaussian functions defined in terms of optical depth. Each individual fit component is shown by a solid color curve, and the overall fit to the absorption profile is shown as a red dashed curve. The resulting fit parameters are presented in Table 1. Note that for the weak absorption of the ν_2 $3_{2,1}$–$3_{1,2}$ transition the line center velocity and Gaussian FWHM for the two absorption components were forced to be the average of those parameters measured for each component from the other two transitions.

Integrated optical depths ($\int \tau dv$) for each component were computed as the area of the Gaussian fitting functions, and are also presented in Table 1. Assuming optically thin absorption (reasonable given $\tau_0 < 1$ and the 3.5 km s^{-1} velocity resolution) column densities in the lower states of the observed transitions are computed as

$$N_{\rm l} = \frac{g_{\rm l}}{g_{\rm u}} \frac{8\pi}{A_{\rm ul}\lambda^3} \int \tau dv, \quad (1)$$

where $g_{\rm l}$ and $g_{\rm u}$ are the lower and upper state statistical weights, $A_{\rm ul}$ is the transition spontaneous emission coefficient, and λ is the transition wavelength. Using the state specific column densities we construct rotation diagrams for the two velocity components where three transitions are observed (8 and 0.5 km s^{-1}). These are presented in Figure 3. Assuming local thermodynamic equilibrium, the 8 km s^{-1} component has a rotational temperature of $T = 57 \pm 2$ K, and a total water column density of $N(\rm H_2O) = (3.67 \pm 0.22) \times 10^{16}$ cm^{-2}, while the 0.5 km s^{-1} component has $T = 82 \pm 3$ K and $N(\rm H_2O) = (4.91 \pm 0.39) \times 10^{16}$ cm^{-2}.

[8] https://www.wavemetrics.com

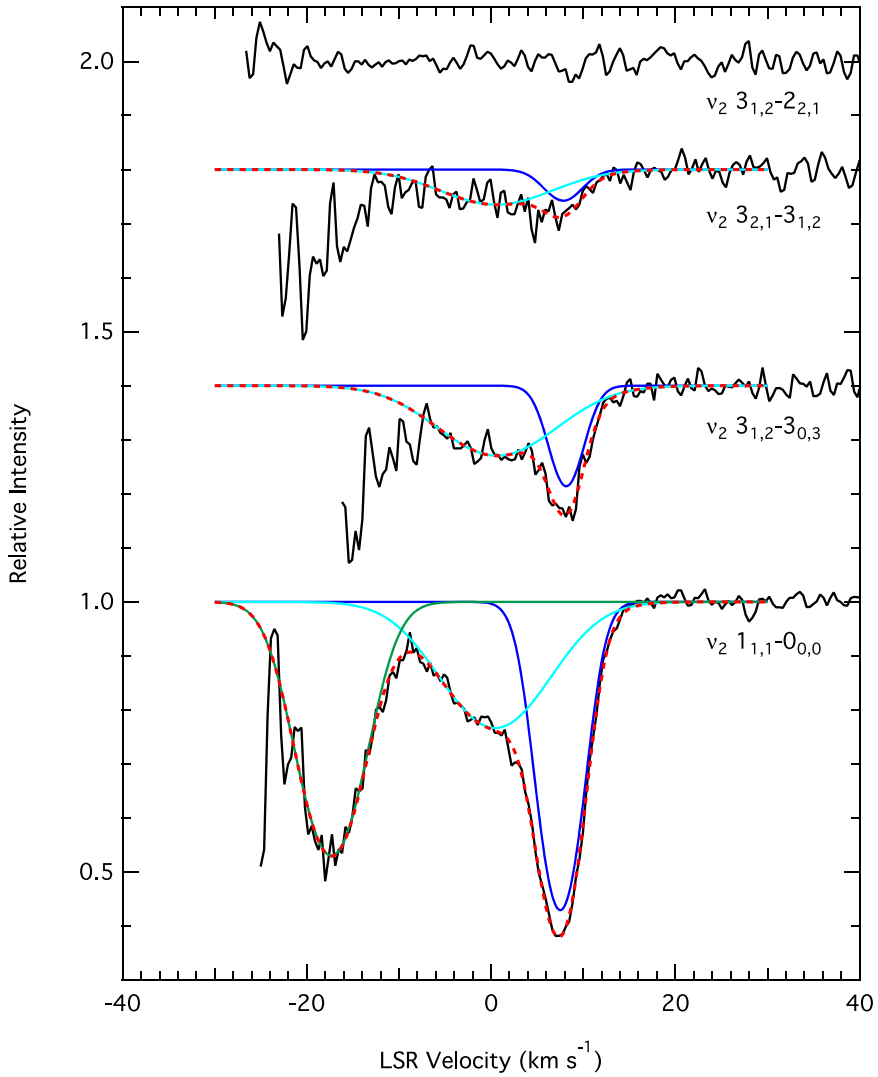

Figure 2. Spectra showing the water absorption lines observed toward BN. Fits to the components at 8, 0.5, and −17 km s^{-1}, are shown by blue, cyan, and green curves, respectively, and the sum of all components is shown as a red dashed curve. The top spectrum shows a non-detection of the transition predicted to have the strongest absorption after the detected transitions in the observed wavelength range (ν_2 $3_{1,2}$–$2_{2,1}$ at 6.1068262 μm). Spectra have been shifted vertically for clarity.

4. Discussion

4.1. Comparison to Previous Near-to-mid–infrared Observations of BN

BN has been the target of several observing campaigns. All three of the velocity components that we observe in H_2O absorption have previously been identified[9] in absorption lines from the $v = 1$–0 bands of ^{12}CO and ^{13}CO at 4.7 μm and the $v = 2$–0 band of ^{12}CO at 2.3 μm (Hall et al. 1978; Scoville et al. 1983; Beuther et al. 2010). Using a rotation diagram analysis similar to that presented above, Scoville et al. (1983) determined that the 8 km s^{-1} component contained total CO column densities of $N(^{12}\mathrm{CO}) = (7.45 \pm 0.3) \times 10^{18}$ cm^{-2} and $N(^{13}\mathrm{CO}) = (7.75 \pm 0.4) \times 10^{16}$ cm^{-2} at a rotational temperature of $T = 150 \pm 10$ K, and that the −17 km s^{-1} component contained total CO column densities of $N(^{12}\mathrm{CO}) = (5.13 \pm 0.3) \times 10^{18}$ cm^{-2} and $N(^{13}\mathrm{CO}) = (5.39 \pm 0.4) \times 10^{16}$ cm^{-2} at a rotational temperature of $T = 150 \pm 30$ K. The spectral resolution of their observations (∼7 km s^{-1}) resulted in the blending of the weaker −3 km s^{-1} component with the other two components, and precluded an independent analysis of this feature. Scoville et al. (1983) also reported components showing weak ^{12}CO absorption at 30 km s^{-1} and ^{12}CO $v = 1$–0 emission at 20 km s^{-1}, neither of which we detect in H_2O.

More recent 4.7 μm CO observations of BN were made using the CRyogenic high-resolution InfraRed Echelle Spectrograph (CRIRES; Käufl et al. 2004) on UT1 at the Very Large Telescope (VLT) at ∼3 km s^{-1} spectral resolution (Beuther et al. 2010). With telluric CO absorption affecting both the −3 and 8 km s^{-1} components, these authors only analyzed the −17 km s^{-1} component, finding $N(^{13}\mathrm{CO}) \approx 5.7 \times 10^{16}$ cm^{-2} at a rotational temperature of $T = 112 \pm 20$ K, in agreement with the previous findings. However, Beuther et al. (2010) did not detect CO absorption at 30 km s^{-1}, and suggested that either the original detection must be a transient feature, or it was insignificant with respect to the continuum S/N level. Emission from both the ^{12}CO and ^{13}CO $v = 1$–0 bands is reported at 20 km s^{-1}, again in agreement with Scoville et al. (1983). While Beuther et al. (2010) interpreted ^{12}CO $v = 1$–0 $R(0)$ emission spatially extended along the slit as arising in an $r \sim 1650$ au

[9] We assume here that the −3 km s^{-1} component reported in CO absorption corresponds to the 0.5 km s^{-1} component identified herein.

Table 1
Absorption Line Parameters

Transition	Wavelength (μm)	E_l/k_b (K)	v_{LSR} (km s^{-1})	FWHM (km s^{-1})	τ_0	$\int \tau dv$ (km s^{-1})	N_l (10^{15} cm^{-2})
$1_{1,1}$–$0_{0,0}$	6.116331	0	7.5	5.3 ± 0.2	0.84 ± 0.02	4.78 ± 0.19	2.35 ± 0.09
$3_{1,2}$–$3_{0,3}$	6.113771	196.8	8.2	4.3 ± 0.3	0.21 ± 0.01	0.95 ± 0.10	1.67 ± 0.17
$3_{2,1}$–$3_{1,2}$	6.075447	249.4	7.8	4.8 ± 0.4	0.06 ± 0.01	0.31 ± 0.05	0.51 ± 0.08
$1_{1,1}$–$0_{0,0}$	6.116331	0	0.4	13.3 ± 0.8	0.27 ± 0.01	3.76 ± 0.25	1.85 ± 0.12
$3_{1,2}$–$3_{0,3}$	6.113771	196.8	0.7	14.7 ± 1.1	0.13 ± 0.01	2.17 ± 0.19	3.82 ± 0.33
$3_{2,1}$–$3_{1,2}$	6.075447	249.4	0.6	14.0 ± 1.3	0.07 ± 0.01	1.00 ± 0.11	1.67 ± 0.20
$1_{1,1}$–$0_{0,0}$	6.116331	0	−17	8.0 ± 0.2	0.63 ± 0.01	5.42 ± 0.16	2.66 ± 0.08

Note. Transition properties, parameters for the Gaussian fits shown in Figure 2, and derived column densities.

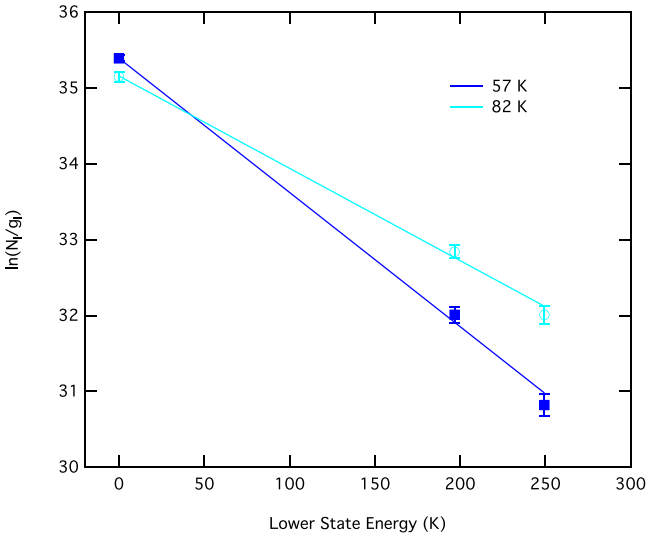

Figure 3. Rotation diagrams for the 8 km s^{-1} component (blue) and 0.5 km s^{-1} component (cyan). Color coding corresponds to the Gaussian fits shown in Figure 2.

circumstellar disk, millimeter continuum images show no evidence for such an extended structure in dust (Rodríguez et al. 2009; Galván-Madrid et al. 2012; Plambeck et al. 2013), and it is unexpected that such a large structure would be retained around BN following its recent dynamical ejection at ∼30 km s^{-1}.

Water absorption from the ν_3 ro-vibrational band near 2.7 μm has also been observed toward BN before using the NASA Kuiper Airborne Observatory. Knacke & Larson (1991) detected absorption from both the −17 and 8 km s^{-1} components in a handful of transitions out of low-lying states—albeit at rather low S/N—and estimated $N(H_2O) = (2 \pm 1) \times 10^{17}$ cm^{-2}, under the assumption that $T = 150$ K. They also note the effects that a lower temperature would have, and give another estimate of $N(H_2O) = (7.7 \pm 3.9) \times 10^{16}$ cm^{-2} if $T = 70$ K. Our new results both confirm these findings and demonstrate the significant improvement achieved with the next generation of airborne observatories.

Ideally, we would compare H_2O and CO abundances in all components that have been observed. However, the lack of a CO analysis for the 0.5 km s^{-1} component, the lack of H_2O data for the −17 km s^{-1} component, and the lack of H_2O emission at 20 km s^{-1}, limit our options here. We can place a lower limit of $N(H_2O)/N(CO) \gtrsim 5 \times 10^{-4}$ in the −17 km s^{-1} component using only the column density measured in the $0_{0,0}$ ground state of water. The 8 km s^{-1} component is the only one where both full CO and H_2O analyses exist, and there we find $N(H_2O)/N(CO) = 5 \times 10^{-3}$. Both of these results are consistent with predictions of chemical models for cool, dense gas (e.g., Doty et al. 2002; Hollenbach et al. 2009), where most water has frozen out onto grains.

Previous low resolution ($R \sim 670$) spectra of BN have in fact revealed broad absorption centered at 3.08 μm due to water ice (Knacke et al. 1982; Smith et al. 1989), and the narrow peak of this absorption feature requires that some amount of the ice be crystalline at $T > 100$ K. The 3 μm ice absorption band presented in Smith et al. (1989) has a peak optical depth of $\tau = 1.78$ and a width of ∼320 cm^{-1}. When a laboratory-measured integrated band strength for the O–H stretch mode in bulk H_2O ice of 2.0×10^{-16} cm per molecule (Hagen et al. 1981) is adopted, this corresponds to an H_2O ice column density of $N(H_2O_{ice}) \approx 2.9 \times 10^{18}$ cm^{-2}. Assuming that the −17 km s^{-1} velocity component has similar excitation conditions and thus water abundance to the other two components, the ratio of water vapor to water ice toward BN is $N(H_2O)/N(H_2O_{ice}) \sim 0.04$. This confirms the scenario where water is predominantly in solid form.

BN has also been observed at $R \sim 1400$ in the mid-infrared (mid-IR) with the *Infrared Space Observatory*–Short Wavelength Spectrometer (*ISO*-SWS; Gonzalez-Alfonso et al. 1998; van Dishoeck et al. 1998). Both studies reported absorption and emission from the ν_2 band of H_2O, but the large SWS aperture (14″ × 20″ at the shortest wavelengths) means that the region surrounding BN, including IRc2, was also contributing to the observed spectra. Our observations rule out BN as the source of the H_2O emission in those spectra, and rule out the three foreground components that we detect in H_2O absorption as giving rise to the H_2O absorption seen in those spectra.

4.2. Nature of the Foreground Components

The total visual extinction toward BN was estimated to be $A_V \approx 17$ mag from observations of the 9.8 μm silicate absorption feature (Gezari et al. 1998). Assuming $N_H/A_V = 1.8 \times 10^{21}$ cm^{-2} mag^{-1} (Bohlin et al. 1978)—where $N_H \equiv N(H) + 2N(H_2)$—this corresponds to a total hydrogen column density of $N_H = 3.1 \times 10^{22}$ cm^{-2}. The fractional abundance of water ice ($X(H_2O_{ice}) \equiv N(H_2O_{ice})/N_H$) averaged over all of the foreground gas is then $X(H_2O_{ice}) \approx 10^{-4}$, in agreement with predictions from photodissociation region (PDR) chemical models (e.g., Hollenbach et al. 2009). It is not possible to determine which of the three foreground components contribute to the H_2O ice absorption signal, nor can any component be ruled out given the

similar excitation conditions inferred from H_2O and CO. Again assuming that the -17 km s^{-1} component has similar $N(H_2O)$ as the other two components, $X(H_2O) \sim 4 \times 10^{-6}$ in the foreground gas.

There is enough material along the line of sight that all three velocity components detected in H_2O absorption can potentially be associated with dense molecular gas ($A_V \gtrsim 5$ mag; Snow & McCall 2006). The depth into a cloud at which water ice becomes a major oxygen reservoir depends on the strength of the ultraviolet (UV) radiation field and gas density, but for much of the parameter space explored by Hollenbach et al. (2009) $X(H_2O_{ice})$ exceeds 10^{-4} for $A_V \gtrsim 3$ mag. In these same models $X(H_2O)$ peaks at about 10^{-7}–10^{-6} in a layer where water ice is being photodesorbed by the impinging far-UV radiation (Melnick et al. 2011). Additionally, X(CO) $\sim 10^{-4}$ at moderate cloud depths ($2 \lesssim A_V \lesssim 4$ mag) before it freezes out onto grains at higher visual extinctions. The observed value of X(CO) averaged over all three cloud components is $\sim 5 \times 10^{-3}$. The peak gas-phase H_2O abundance occurs farther into the cloud than the peak CO abundance, so it is expected that H_2O probes a region with lower gas temperature, in agreement with our findings.

The H_2O and CO observations suggest that the line of sight toward BN intersects three distinct clouds, all of which have fairly similar physical conditions ($n \sim 10^4$–10^5 cm^{-3}, total $A_V \sim 5$ mag, $T \sim 60$–150 K). Given the limited range of A_V available per cloud, the PDR models in Hollenbach et al. (2009) favor a UV radiation field of order 100 times the average local interstellar radiation field (parameterized as $G_0 = 1$; Habing 1968) in order to roughly match the observed gas phase CO and H_2O ice abundances. These estimates are well below the extreme conditions ($G_0 \gtrsim 10^4$, $T \gtrsim 500$ K) inferred from atomic and molecular emission line observations in the BN/KL and Trapezium regions (e.g., Melnick et al. 2011; Goicoechea et al. 2015a, 2015b), and our H_2O observations must be tracing a different physical component. Water emission observed toward the nearby Orion KL region at high spectral resolution with *Herschel*/Heterodyne Instrument for the Far Infrared does not show any components that correspond with our observations (Melnick et al. 2010). While the "extended warm gas" component matches the kinematics of our 8 km s^{-1} component, it has an H_2O column density over 100 times larger than what we have inferred. The H_2O and CO absorption could be associated with individual narrow streamers in the explosive outflow observed in CO emission (Bally et al. 2017). Indeed, the lack of redshifted (with respect to the Orion molecular cloud) absorption toward BN could suggest that it lies near the center of the explosive outflow, as would be expected if it played some part in triggering the event. Verification of this potential association would require a kinematic analysis of the CO streamers directly in front of BN. It is not trivial to relate the three foreground clouds seen toward BN with molecular emission previously observed in the region, and they may be associated with gas that is not easily traceable via emission in a crowded environment where many sources experience more extreme conditions.

4.3. Lack of Water in the Vicinity of BN

The radial velocity of BN has been best constrained by observations of hydrogen recombination lines arising from a hypercompact H II region (Rodríguez et al. 2009; Plambeck et al. 2013). In particular, Plambeck et al. (2013) reported $v_{LSR} = 23.2 \pm 0.5$ km s^{-1} from observations of the H30α line at 232 GHz. The CO $v = 1$–0 emission detected by Scoville et al. (1983) and Beuther et al. (2010) is consistent with this velocity, hence both studies associated the emission with the immediate vicinity of BN. We detect neither emission nor absorption from H_2O at the BN radial velocity. The lack of H_2O absorption—and of CO absorption—at 23 km s^{-1}, and the relatively low temperatures ($T \leqslant 150$ K) inferred from H_2O and CO absorption at other velocities, indicates that there is no molecular foreground gas in close proximity to BN.

If BN has a circumstellar disk it must be very compact, as mm continuum observations show the object to be a point source at $0\farcs15$ ($\sim$60 au) angular resolution (Rodríguez et al. 2009; Galván-Madrid et al. 2012; Plambeck et al. 2013). It must also be oriented in such a way as to not cover the mid-IR continuum source, as that would presumably cause CO and H_2O absorption. This would seem to disfavor the disk interpretation of near-IR imaging polarimetry observations proposed by Jiang et al. (2005), and the large disk proposed by Beuther et al. (2010). However, the properties of the region giving rise to CO $v = 1$–0 emission proposed by Scoville et al. (1983) are consistent with the mm observations. It is possible that H_2O also resides in this region, but that its emission is too weak to be detected by our observations. Because quantitative speculation about such unobserved H_2O emission requires knowledge of several poorly constrained parameters (gas distribution, gas density, temperature, radiation field), we make no attempt to do so here.

5. Summary

We have observed BN at 6 μm and detected absorption from H_2O arising in cool ($T \sim 70$ K), dense foreground clouds. The abundance ratios between water and CO, $N(H_2O)/N(CO) = 5 \times 10^{-3}$, and between water vapor and water ice, $N(H_2O)/N(H_2O_{ice}) \sim 0.04$, are indicative of a PDR environment where H_2O is released from ice mantles in a thin photodesorption layer. Neither H_2O absorption nor emission are detected at the systemic velocity of BN, adding further constraints to the size and orientation of any potential circumstellar disk. The non-detection of H_2O in close proximity to BN adds new information regarding its current state, and should be accounted for in dynamical ejection models. For example, if BN was recently in a protostellar phase just before ejection, then either all of the dense gas must have been stripped away, or since accreted onto the star, or be oriented so as not to produce significant infrared absorption. In contrast, source I has retained a massive, Keplerian accretion disk (e.g., Hirota et al. 2014; Ginsburg et al. 2018). Finally, we note that BN may serve as a good sight line for studying molecular absorption at infrared wavelengths arising from cool, dense gas within the Orion molecular cloud. Over time, it may also enable the study of cloud structure in the plane of the sky as BN's high proper motion changes the foreground gas observed along the line of sight at different epochs.

Based on observations made with the NASA/DLR Stratospheric Observatory for Infrared Astronomy (SOFIA). SOFIA is jointly operated by the Universities Space Research Association, Inc. (USRA), under NASA contract NNA17BF53C, and the Deutsches SOFIA Institut (DSI) under DLR contract 50 OK 0901 to the University of Stuttgart. (Financial support for this work was provided by NASA through award #04-0120 issued by USRA.)

ORCID iDs

Nick Indriolo https://orcid.org/0000-0001-8533-6440

References

Allen, D. A., & Burton, M. G. 1993, Natur, 363, 54
Bally, J., Ginsburg, A., Arce, H., et al. 2017, ApJ, 837, 60
Bally, J., & Zinnecker, H. 2005, AJ, 129, 2281
Becklin, E. E., & Neugebauer, G. 1967, ApJ, 147, 799
Beuther, H., Linz, H., Bik, A., Goto, M., & Henning, T. 2010, A&A, 512, A29
Bohlin, R. C., Savage, B. D., & Drake, J. F. 1978, ApJ, 224, 132
Boonman, A. M. S., & van Dishoeck, E. F. 2003, A&A, 403, 1003
Chatterjee, S., & Tan, J. C. 2012, ApJ, 754, 152
Clarke, M., Vacca, W. D., & Shuping, R. Y. 2015, in ASP Conf. Ser. 495, Astronomical Data Analysis Software and Systems XXIV (ADASS XXIV), ed. A. R. Taylor & E. Rosolowsky (San Francisco, CA: ASP), 355
Cushing, M. C., Vacca, W. D., & Rayner, J. T. 2004, PASP, 116, 362
Doty, S. D., van Dishoeck, E. F., van der Tak, F. F. S., & Boonman, A. M. S. 2002, A&A, 389, 446
Farias, J. P., & Tan, J. C. 2018, A&A, 612, L7
Galván-Madrid, R., Goddi, C., & Rodríguez, L. F. 2012, A&A, 547, L3
Gezari, D. Y., Backman, D. E., & Werner, M. W. 1998, ApJ, 509, 283
Ginsburg, A., Bally, J., Goddi, C., Plambeck, R., & Wright, M. 2018, ApJ, 860, 119
Goicoechea, J. R., Chavarría, L., Cernicharo, J., et al. 2015a, ApJ, 799, 102
Goicoechea, J. R., Teyssier, D., Etxaluze, M., et al. 2015b, ApJ, 812, 75
Gonzalez-Alfonso, E., Cernicharo, J., van Dishoeck, E. F., Wright, C. M., & Heras, A. 1998, ApJL, 502, L169
Habing, H. J. 1968, BAN, 19, 421
Hagen, W., Tielens, A. G. G. M., & Greenberg, J. M. 1981, CP, 56, 367
Hall, D. N. B., Kleinmann, S. G., Ridgway, S. T., & Gillett, F. C. 1978, ApJL, 223, L47
Hirota, T., Kim, M. K., Kurono, Y., & Honma, M. 2014, ApJL, 782, L28
Hollenbach, D., Kaufman, M. J., Bergin, E. A., & Melnick, G. J. 2009, ApJ, 690, 1497
Indriolo, N., Neufeld, D. A., DeWitt, C. N., et al. 2015, ApJL, 802, L14
Jiang, Z., Tamura, M., Fukagawa, M., et al. 2005, Natur, 437, 112
Käufl, H., Ballester, P., Biereichel, P., et al. 2004, Proc. SPIE, 5492, 1218
Knacke, R. F., & Larson, H. P. 1991, ApJ, 367, 162
Knacke, R. F., McCorkle, S., Puetter, R. C., Erickson, E. F., & Kraetschmer, W. 1982, ApJ, 260, 141
Kounkel, M., Hartmann, L., Loinard, L., et al. 2017, ApJ, 834, 142
Luhman, K. L., Robberto, M., Tan, J. C., et al. 2017, ApJL, 838, L3
McCall, B. J. 2001, PhD thesis, Univ. Chicago
Melnick, G. J., Tolls, V., Neufeld, D. A., et al. 2010, A&A, 521, L27
Melnick, G. J., Tolls, V., Snell, R. L., et al. 2011, ApJ, 727, 13
Menten, K. M., Reid, M. J., Forbrich, J., & Brunthaler, A. 2007, A&A, 474, 515
Plambeck, R. L., Bolatto, A. D., Carpenter, J. M., et al. 2013, ApJ, 765, 40
Richter, M. J., Ennico, K. A., McKelvey, M. E., & Seifahrt, A. 2010, Proc. SPIE, 7735
Rodríguez, L. F., Poveda, A., Lizano, S., & Allen, C. 2005, ApJL, 627, L65
Rodríguez, L. F., Zapata, L. A., & Ho, P. T. P. 2009, ApJ, 692, 162
Scoville, N., Kleinmann, S. G., Hall, D. N. B., & Ridgway, S. T. 1983, ApJ, 275, 201
Smith, R. G., Sellgren, K., & Tokunaga, A. T. 1989, ApJ, 344, 413
Snow, T. P., & McCall, B. J. 2006, ARA&A, 44, 367
Tan, J. C. 2004, ApJL, 607, L47
van Dishoeck, E. F., Wright, C. M., Cernicharo, J., et al. 1998, ApJL, 502, L173
Young, E. T., Becklin, E. E., Marcum, P. M., et al. 2012, ApJL, 749, L17